Scripta Materialia 177 (2020) 146–150

Contents lists available at ScienceDirect

Scripta Materialia

journal homepage: www.elsevier.com/locate/scriptamat

Three-dimensional hierarchical nanoporous copper via direct ink writing and dealloying

Shahryar Mooraj[a], Samuel S. Welborn[b,e], Shuyang Jiang[a,c], Siyuan Peng[a], Jintao Fu[b], Sarah Baker[d], Eric B. Duoss[d], Cheng Zhu[d], Eric Detsi[b,e,*], Wen Chen[a,*]

[a] Department of Mechanical and Industrial Engineering, University of Massachusetts, Amherst, MA 01003-2210, USA
[b] Department of Materials Science & Engineering, University of Pennsylvania, Philadelphia, PA 19104-6272, USA
[c] Smith College, Northampton, MA 01063, USA
[d] Lawrence Livermore National Laboratory, 7000 East Avenue, Livermore, CA 94550, USA
[e] Vagelos Institute for Energy Science and Technology (VIEST), Philadelphia, PA 19104, USA

ARTICLE INFO

Article history:
Received 11 September 2019
Revised 8 October 2019
Accepted 9 October 2019

Keywords:
3D printing
Additive manufacturing
Direct ink writing
Hierarchical nanoporous Cu
Dealloying

ABSTRACT

Three-dimensional (3D) hierarchical nanoporous Cu (3DHNP-Cu) is synthesized using a combination of direct ink writing (DIW) based 3D printing, thermal sintering, and chemical dealloying of Mn–Cu alloys. Through tuning processing conditions such as ink composition and cooling rate (after sintering), with consideration of Mn loss during sintering, 3DHNP-Cu with fully bicontinuous nanostructures and negligible residual Mn can be produced after dealloying. The 3DHNP-Cu is comprised of structural features that span seven orders of magnitude, where DIW digitally controls macroscale porous features, thermal sintering and degradation of the binding polymer determines microscale porous features, and dealloying gives rise to nanoscale pores.

Due to their high surface area-to-volume ratio and unique size-dependent properties, three dimensional (3D) bulk nanoporous metals are promising materials for various applications such as (electro)catalysis [1–4], battery electrodes [5–7], fuel cells [8,9], supercapacitors [10,11], sensors and actuators [12–14]. A common method to manufacture 3D bulk nanoporous metals is by dealloying, the selective leaching of the most chemically active phase in a parent alloy. Various dealloying strategies have been used depending on the reactivity of the system: (a) Less reactive systems such as nanoporous Au, Pt, Ag, Cu, Sn, and Ni are commonly made in aqueous media through conventional free corrosion dealloying [12,15–18], or during electrolytic dealloying where an external bias voltage is used to remove the sacrificial phase [19–23], (b) Reactive and refractory nanoporous materials such as nanoporous Ti, Sb, Mo, and Nb are usually produced through free corrosion by metallic melt, a leaching process where a molten metal is used to selectively extract the most reactive component in a parent alloy, leveraging differences in enthalpy of mixing between the alloy elements and the molten metal [24–30], (c) Sacrificial elements with high vapor pressure can also be removed by thermal evaporation [31,32]. (d) Finally, for several energy applications such as non-aqueous alkali and alkaline earth metal batteries, non-precious, oxide-free 3D nanoporous materials are needed. In this case, dealloying is carried out in inert environments and non-aqueous solutions. For instance, Sieradzki and Chen demonstrated electrolytic dealloying in non-aqueous electrolyte with Li^+ as the working ion [33]. Recently, Corsi et al. demonstrated the fabrication of ultrafine, oxide-free 3D bulk nanoporous Al from Al–Mg parent alloys for on-demand hydrogen production by hydrolysis in neutral water [3,34]. These efforts suggest the possibility to use dealloying to manufacture 3D bulk nanoporous materials with nearly any practical element. Moving forward, a topic that is not yet mastered is the development of 3D bulk nanoporous materials with multiple length scale structures. Various strategies have been proposed, such as a two-step dealloying route to make a bulk nested-network of nanoporous gold [35], a single-step dealloying route layered nanoporous metals using parent alloys with engineered defects [12], and single-step dealloying route to hierarchical bulk nanoporous metals using parent alloys with dual-phase structures [3,4]. In recent years, laser-based additive manufacturing has been employed to manufacture macroporous alloys, which can be dealloyed to introduce a second level of porosity [36–38]. In particular, Zhang et al. [37] used selective laser melting (SLM) to print a Cu–Mn alloy, and dealloyed it to produce 3D hierarchical

* Corresponding authors.
E-mail addresses: detsi@seas.upenn.edu (E. Detsi), wenchen@umass.edu (W. Chen).

https://doi.org/10.1016/j.scriptamat.2019.10.013
1359-6462/

nanoporous Cu (3DHNP-Cu) with an average pore size of ~140 nm. Although viable to produce 3DHNP-Cu, SLM based methods require high energy and operation costs. While the macroscale pores were controlled by the printing process, the microscale pores formed accidentally by micro-cracking through thermal residual stresses during SLM [37]. The rapid and highly localized heating and cooling along with the moving melt pools during SLM induce thermal residual stresses, which often cause distortion or even micro-cracking of the parts [39]. Such destructive stresses are often site and geometry specific, and the complex thermo-physical process of laser-powder interaction makes this process control and optimization difficult.

Here we introduce a novel approach to fabricating well-controllable 3DHNP-Cu via a 3-step process: (i) direct ink writing (DIW) based additive manufacturing of Mn and Cu bi-materials; (ii) thermal sintering of these materials to produce 3D Mn–Cu alloy architectures; (iii) dealloying of the Mn–Cu alloy in aqueous hydrochloric acid (HCl) solution to form self-supporting bulk 3DHNP-Cu architectures. The eventual 3DHNP-Cu is comprised of pores on multiple length scales: macroscopic pores of 0.1–1 mm built by the DIW process, micrometer-sized pores of 1–10 µm formed due to the evaporation of solvents and the degradation of the polymer binder during sintering, and nanoscale pores of 10–100 nm by dealloying.

DIW is an emerging low-cost additive manufacturing technique that enables 3D printing of materials into complex architectures with high fidelity. During DIW, structures are built layer-by-layer through filamentary deposition of colloidal particle or polymer-based inks [40]. A key step of this technique is the development of inks with the appropriate rheological properties so they can flow through a fine-tipped micro-nozzle to form continuous filaments under constant pressure or displacement rate and solidify upon exiting to retain their shape. In this study, building upon our recent work on 3DHNP-Au [38], we developed an ink formulation comprised of Mn and Cu micro-powders, solvents, and polymer binder. The Mn–Cu bi-material inks were prepared by mixing pure elemental powders of Mn and Cu (APS 10 µm, >99.6%, Alfa Aesar) with a PMMA-PnBA bi-block co-polymer binder and organic solvents of Tetrahydrofuran (THF) and 2-Butoxyethanol. Two different inks with overall compositions of $Mn_{70}Cu_{30}$ (at.%) and $Mn_{80}Cu_{20}$ (at.%) were prepared. The volumetric ratio of metal powders to binding polymer in the ink was kept at 7:3. The inks show a typical shear thinning characteristic with an appropriate viscosity range of $10–10^3$ Pa•s that facilitates DIW (Fig. S1). To create 3D architectures, we loaded the ink into a syringe-barrel (Nordson EFD) and pressurized the printhead to deposit ink through a tapered nozzle onto a planar alumina substrate under digital control. Samples of 5 mm × 5 mm × 1.2 mm were printed with an individual layer height of 150 µm at a printing speed of 5 mm/s. Larger samples were also printed for demonstration (Fig. 1). The as-printed parts consisted of discrete Mn and Cu particles bound by the block co-polymer. To form homogeneous Mn–Cu alloy architectures, multi-step heat treatment of the printed samples was carried out in an OTF-1200X tube furnace (MTI Corporation) to a peak temperature of about $0.95T_m$, where T_m is the equilibrium melting temperature of the specific alloy composition and is estimated to be 1223 K and 1292 K for $Mn_{70}Cu_{30}$ and $Mn_{80}Cu_{20}$, respectively [41,42]. The samples were first heated to 373 K for 1 h to remove the THF solvent and subsequently heated to 493 K for 1 h to evaporate the 2-Butoxyethanol. Afterwards, they were heated to 693 K for decomposition of the polymer binder, followed by final sintering at 1173 K and 1239 K for $Mn_{70}Cu_{30}$ and $Mn_{80}Cu_{20}$, respectively for 15 h. The heating rate between each step was 5 K/min. Based on Fick's Law, the diffusion length $L=(2D\cdot t)^{1/2}$, where D is the diffusion coefficient and t is time. $D \approx 1.02 \times 10^{-4}\ e^{(-200\text{KJ mol}^{-1}/\text{RT})}\ \text{m}^2\ \text{s}^{-1}$ for the Mn–Cu system, where R is the ideal gas constant and T is the

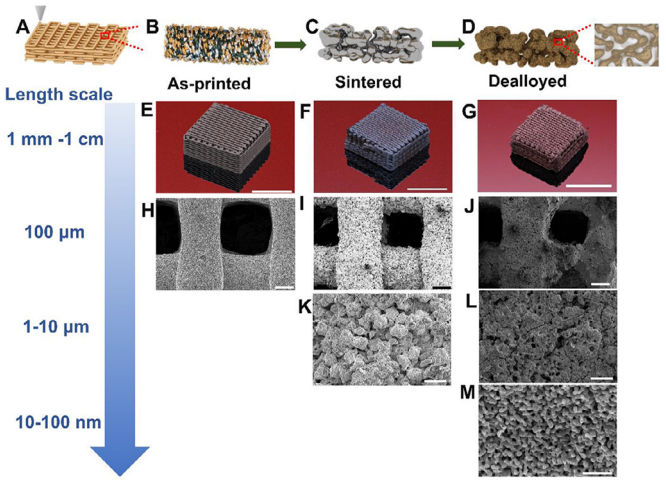

Fig. 1. Evolution of the structural features at different length scales in the 3DHNP-Cu throughout the processing steps. (A–B) Schematic illustrations of DIW of bi-material inks composed of Cu and Mn mixed powders, polymer binder, and solvents. DIW digitally dictates the macroscale porosity. (C) Thermal sintering leads to alloying of Mn and Cu, evaporation of the solvents, and decomposition of the polymer binder to yield microscale porosity. (D) Dealloying step selectively removes Mn to yield the nanoscale porosity. Optical images of the mm–cm scale multilayer woodpile-like architectures at different states of as-printed (E), sintered (F), and dealloyed (G). The scale bars in (E–G) are 10 mm. SEM images are shown depicting the structural evolution after printing, thermal sintering, and dealloying steps for (H–J) the scale bars are 100 µm, for (K–L) the scale bars are 20 µm and for (M) the scale bar is 400 nm.

sintering temperature [43]. Using these values, we can quantitively estimate the diffusion lengths for Mn in $Mn_{70}Cu_{30}$ and $Mn_{80}Cu_{20}$ to be 117 µm and 202 µm, respectively, both are an order of magnitude greater than the ink particle size of ~10 µm. As such, a homogeneous alloy can be achieved after sintering. Upon completion of sintering, samples were either water-quenched or furnace-cooled. The sintered 3D Mn–Cu alloy architectures were subsequently dealloyed for 91.5 h in 0.1M HCl plus 12.5 h in 4M HCl. This two-stage chemical dealloying was used to prevent initial collapse in high concentration media by slowly dealloying the sample in 0.1M HCl to a state where the bubble formation was steady to prevent damage and to avoid severe coarsening of the nanostructures in low concentration media via impractically long dealloying time by switching to 4M HCl to remove Mn quickly [44].

The morphology and chemical composition of the samples were characterized using a Magellan 400 field emission scanning electron microscope (SEM, FEI) equipped with energy-dispersive X-ray spectroscopy (EDS). The crystal structures of the sintered samples were confirmed by X-ray diffraction (XRD). To quantitatively confirm the average nanopore size within the dealloyed 3DHNP-Cu, small-angle X-ray scattering (SAXS) was performed at the Penn Dual Source and Environmental X-Ray Scattering facility that can probe length scales from 1 Å to 570 nm [45].

3DHNP-Cu samples were synthesized by the successive procedures of DIW, thermal sintering, and dealloying (Fig. 1). The 3DHNP-Cu exhibits a hierarchical structure that spans seven orders of magnitude – from centimeters to nanometers. The macroscopic pores are controlled by the DIW process and is hence the most deterministic in its morphology and spatial distribution. The resolution of the macroscopic features is defined by the filament size, which is on the order of 100 µm in the present study (Fig. 1H–J). This minimum feature size depends on both the ink particle size and the rheology, and may be reduced if smaller particles (e.g. nanoparticles) are used. The micrometer-sized pores in the range of ~1–10 µm arise from solvent evaporation and decomposition of the polymer binder (Fig. 1K–L). The distribution and morphology

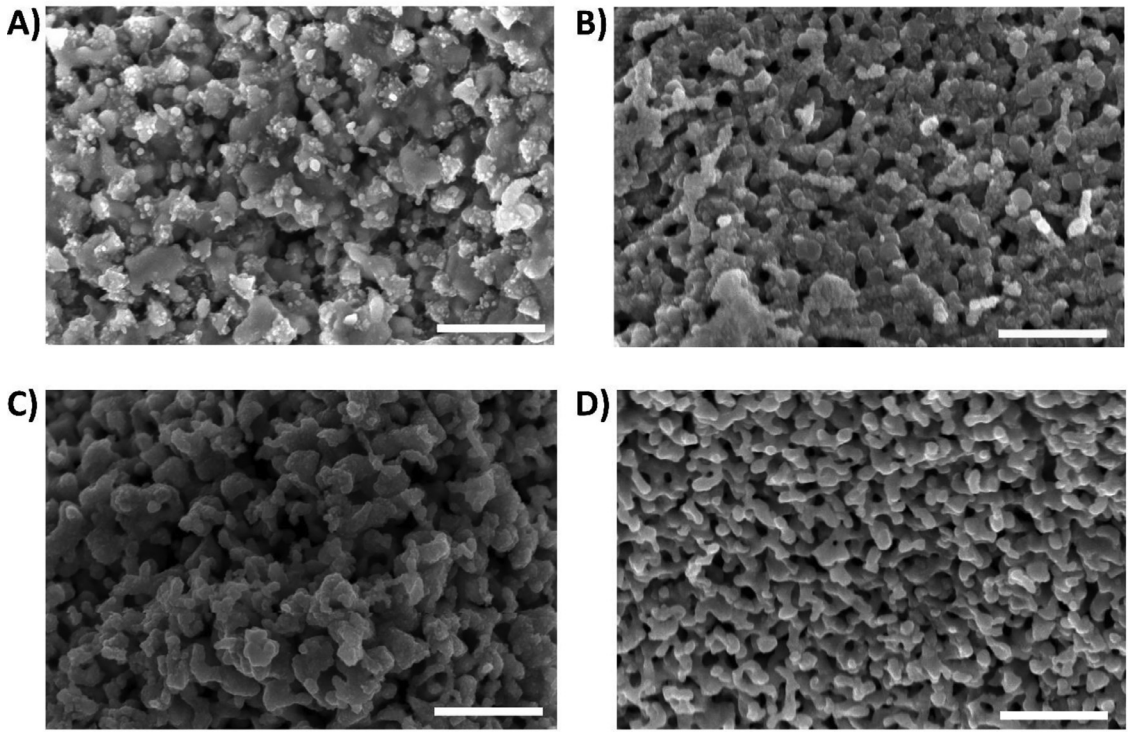

Fig. 2. SEM images of the nanoporous structure of dealloyed 3DHNP-Cu with different starting ink compositions and cooling rates after sintering. (a) $Mn_{70}Cu_{30}$, furnace-cooled; (b) $Mn_{70}Cu_{30}$, water-quenched; (c) $Mn_{80}Cu_{20}$, furnace-cooled; (d) $Mn_{80}Cu_{20}$, water-quenched. Scale bar: 400 nm. These images clearly show the effect of cooling rate on final morphology. Both furnace-cooled samples showed a coarsened microstructure with highly non-smooth and discontinuous ligaments. The water-quenched samples showed smooth and bicontinuous nanopores after dealloying.

Table 1
Composition (at.%) and processing conditions of all considered samples.

Ink composition	Cooling condition	Composition after sintering	Surface composition after dealloying	Interior composition after dealloying
$Mn_{70}Cu_{30}$	Furnace-cooled	$Mn_{51}Cu_{49}$	Mn_5Cu_{95}	Mn_7Cu_{93}
$Mn_{70}Cu_{30}$	Water-quenched	$Mn_{56}Cu_{44}$	$Mn_{13}Cu_{87}$	$Mn_{12}Cu_{88}$
$Mn_{80}Cu_{20}$	Furnace-cooled	$Mn_{76}Cu_{24}$	Cu	Cu
$Mn_{80}Cu_{20}$	Water-quenched	$Mn_{77}Cu_{23}$	Cu	Cu

of these microscale pores may be tuned by adjusting the volume fractions of the solvents and polymer binder provided that an appropriate viscosity with a shear-thinning characteristic is met to maintain the printability of the ink [46]. These macro- and microscopic pores can facilitate high mass-transport throughout the 3DHNP-Cu to expedite reaction kinetics [37].

Thermal sintering produces a homogeneous Mn–Cu alloy from the constituent Mn and Cu micro-particles (Fig. 1K–L) and the subsequent dealloying process creates nanoscale pores of ~60 nm (Fig. 1M). The morphology of these nanoscale pores is typically affected by dealloying conditions, such as dealloying media and time [44]. Here, we reveal that under identical dealloying conditions, the starting ink composition and the cooling rate post-sintering of the Mn–Cu alloy also significantly impact the resultant nanoscale morphology of the 3DHNP-Cu (Fig. 2). Specifically, for furnace-cooled $Mn_{70}Cu_{30}$ and $Mn_{80}Cu_{20}$, the nanoscale ligaments after dealloying were drastically coarsened and became highly non-smooth and discontinuous (Fig. 2a and c), which reduced the reactive surface area. For water-quenched $Mn_{70}Cu_{30}$ and $Mn_{80}Cu_{20}$, smooth and bicontinuous nanoscale pores were evident after dealloying (Fig. 2b and d). From Fig. 2, it is clear that the cooling rate significantly affects the morphology of the nanostructures whereas the effect of starting ink composition is more subtle and will be discussed later. From statistical analysis of the pore distribution with ImageJ, the nano-ligament size of the water-quenched $Mn_{70}Cu_{30}$ and $Mn_{80}Cu_{20}$ was approximately 80 nm and 66 nm, respectively. More interestingly, further chemical composition analysis via EDS revealed considerable residual Mn for both furnace-cooled and water-quenched $Mn_{70}Cu_{30}$ samples (Table 1). To understand the underlying origin, we examined the composition of the as-sintered $Mn_{70}Cu_{30}$ alloy and surprisingly found that the compositions deviate from the nominal composition of $Mn_{70}Cu_{30}$ by a remarkable loss of ~55% and ~45% Mn, i.e. $Mn_{51}Cu_{49}$ and $Mn_{56}Cu_{44}$, for the furnace-cooled and water-quenched samples, respectively (Table 1). It is widely recognized that for dealloying of a binary alloy, the more reactive element should be at least 60 at. % to achieve nearly complete dealloying [47]. Otherwise, the residual reactive element will be less accessible during dealloying, as it does not form a percolating network within the alloy [48], as in the case of the sintered $Mn_{70}Cu_{30}$ here. Mn is a volatile metal with high vapor pressure at elevated temperatures, and adding extra Mn is often used to compensate the evaporation-induced loss in heating of Mn-containing alloys [49]. Here, for the nominal $Mn_{80}Cu_{20}$ ink, $Mn_{76}Cu_{24}$ and $Mn_{77}Cu_{23}$ were measured for the furnace-cooled and water-quenched samples after sintering, respectively. Such compositions are appropriate towards complete dealloying with marginal Mn residue (Table 1). In order for Mn to evaporate, a directional diffusion from interior of the sample towards the outer surface is required. However, the activation energy of diffusion of Mn increases greatly at the composition

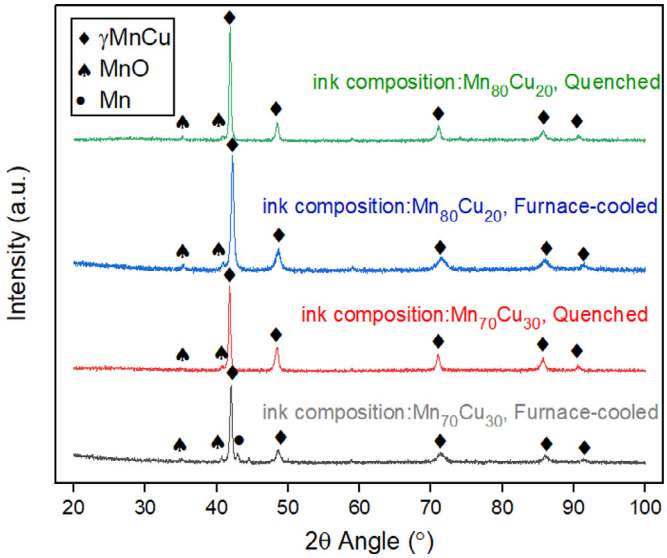

Fig. 3. XRD patterns of all considered Mn–Cu alloys after sintering. All the samples have a γ-MnCu fcc phase with some minor MnO phase. The furnace-cooled $Mn_{70}Cu_{30}$ sample shows a secondary Mn phase as the low cooling-rate allowed some Mn to precipitate out during furnace-cooling.

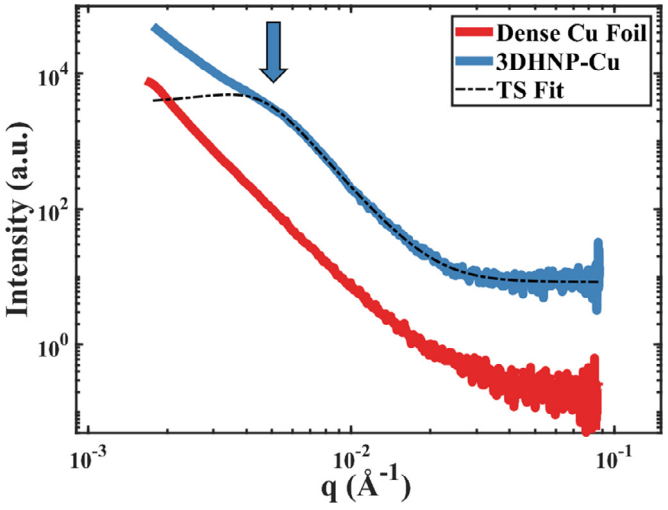

Fig. 4. SAXS patterns of 3DHNP-Cu and dense Cu. The SAXS pattern of the dense Cu shows a straight line with no noticeable peaks, whereas that of the 3DHNP-Cu shows a peak at a q-value of approximately 0.005 Å^{-1}. We fit the 3DHNP-Cu data to the Teubner–Strey model with a constant background, yielding a ligament-to-ligament distance d of ~150 nm.

of $Mn_{80}Cu_{20}$ [50] and thus there is far less Mn available at the immediate surface of the sample for evaporation to take place. The different potency in Mn evaporation of different alloy compositions suggest that the starting ink composition indirectly impacts the eventual morphology in local regions, in which the electrolyte accessibility is hindered. In addition, it is worth noting that while the furnace-cooled $Mn_{80}Cu_{20}$ sample was fully dealloyed, the resulting nanoscale ligaments are less refined than those of the water-quenched $Mn_{80}Cu_{20}$ (Fig. 2c and d). This is likely attributed to prolonged grain growth during cooling that leads to a coarser microstructure in the furnace-cooled sample.

To explore the structural and phase evolution after sintering, XRD was performed. Based on the phase diagram of MnCu (Fig. S2), a secondary Mn phase forms for adequately slow cooling rates. Such a solid-state phase transformation is related to the competition between the thermodynamic driving force and the kinetic barrier to phase decomposition into pure Mn. From the XRD patterns, we found that water-quenching prevents the formation of pure Mn in both $Mn_{70}Cu_{30}$ and $Mn_{80}Cu_{20}$ samples (Fig. 3). However, a noticeable amount of secondary Mn phase was detected in the furnace-cooled $Mn_{70}Cu_{30}$, while the furnace-cooled $Mn_{80}Cu_{20}$ was single-phase FCC MnCu (Fig. 3). This may again be attributed to increased activation energy for diffusion at higher Mn contents in the Mn–Cu alloy system [50]. A higher activation energy reduces the kinetic favorability for secondary phases to form, as Mn is less likely to precipitate from the solid solution. In addition, some MnO was identified for all considered samples (Fig. 3), suggesting oxidation of the samples during thermal sintering despite continuous flow of protective argon.

From the above considerations, the 3DHNP-Cu fabricated from dealloying of the water-quenched $Mn_{80}Cu_{20}$ shows both desirable morphology and composition. SAXS, a reciprocal space technique that provides statistically representative information about feature sizes from ~1 to 100 nm [45,51] was performed to further quantify the morphology of the nanoscale pores in this sample. The SAXS patterns of 3DHNP-Cu and dense Cu foil are compared in Fig. 4, SAXS intensity vs. q. Here, $q = 4\pi sin(\theta)/\lambda$, where 2θ is the angle between the incident beam and the scattered waves measured at the detector, and λ is the wavelength of the X-rays. The data extend to a q-value of approximately 10^{-3} Å^{-1}, nearing our instrument's resolution (~600 nm in real space). Clearly, the pattern of the dense Cu shows a straight line, indicating an absence of repetitive or quasi-repetitive nanostructure. In contrast, the SAXS pattern of the 3DHNP-Cu shows a peak at approximately 0.005 Å^{-1} (highlighted by the arrow in Fig. 4). To ascertain a characteristic size for these ligaments, we fit the pattern of 3DHNP-Cu in the region 0.004 Å^{-1} $< q <$ 0.08 Å^{-1} with the Teubner–Strey model (with a constant background) [45,52], the black dashed curve in Fig. 4. The model's fit parameters, the ligament-to-ligament distance d and correlation length ξ, were determined to be $d = 1527$ Å (~150 nm), and $\xi = 447$ Å (~45 nm). Since d is a measure of the ligament-to-ligament distance, the average ligament and pore diameters can be calculated if the nano-pore void fraction is known. Although we have not measured this, we estimate it to be between 50 and 65%, corresponding to a nano-ligament size of 75 and 54 nm, respectively. This result agrees well with the SEM images of the nanopore morphology (Fig. 2D). The presence of these nanoscale pores significantly increases the surface area of the 3DHNP-Cu and provide more active sites to participate in catalysis of relevant reactions.

In this work, we developed a novel method to produce 3DHNP-Cu by DIW of Mn–Cu alloys, thermal sintering, and dealloying. This approach allows control of the 3D structure of Cu over multiple length scales. In our approach, DIW enables digital control of the macroscale porosity and geometry, thermal sintering produces homogeneous alloys with microscale pores via thermal evaporation of solvents and degradation of the binding polymer, and dealloying introduces nanoscale pores into the system. In addition, we revealed that both volatilization of Mn during sintering, and rate of cooling should be considered carefully, as they play critical roles in alloy composition and phase formation, which affects the nanoscale pore morphology of the resultant 3DHNP-Cu after dealloying. This work provides a pathway for creating 3DHNP-Cu and widens the design toolbox for 3D printing of hierarchical nanoporous metals for myriad applications.

Declaration of Competing Interest

The authors declare that they have no known competing financial interests or personal relationships that could have appeared to influence the work reported in this paper.

Acknowledgments

This work was performed under the auspices of the U.S. Department of Energy by Lawrence Livermore National Laboratory under Contract DE-AC52-07NA27344 and partially funded by the Laboratory Directed Research and Development project 19-SI-005 and University of Massachusetts Faculty Startup Fund. The authors are also thankful to the VIEST for the support through the 2019 VIEST Graduate Fellowship support and the use of the Dual Source and Environmental X-ray Scattering facility operated by the Laboratory for Research on the Structure of Matter at Penn (NSF MRSEC 17-20530). The equipment purchase was made possible by an NSF MRI grant (17-25969), an ARO DURIP grant (W911NF-17-1-0282). This work benefited from the use of the SasView application, originally developed under NSF award DMR-0520547. S.M., C. Z., and W.C. designed the ink and performed the direct ink writing, S.S.W. carried out the SAXS measurements and drafted the section on SAXS, S.M., J.F., and E.D. designed the dealloying protocol, S.M. and W.C. drafted the initial manuscript, E.D wrote the core of the introduction, E.D and W.C. designed the key experiments and supervised the project. All authors contributed to the data analysis, discussion, and manuscript writing. LLNL-JRNL-789328.

Supplementary materials

Supplementary material associated with this article can be found, in the online version, at doi:10.1016/j.scriptamat.2019.10.013.

References

[1] E. Detsi, J.B. Cook, B.K. Lesel, C.L. Turner, Y.-L. Liang, S. Robbennolt, S.H. Tolbert, Energy Environ. Sci. 9 (2016) 540–549.
[2] A. Pröschel, J. Chacko, R. Whitaker, M.A.U. Chen, E. Detsi, J. Electrochem. Soc. 166 (2019) H146–H150.
[3] J.S. Corsi, J. Fu, Z. Wang, T. Lee, A.K. Ng, E. Detsi, ACS Sustain. Chem. Eng. (2019).
[4] J. Fu, Z. Deng, T. Lee, J.S. Corsi, Z. Wang, D. Zhang, E. Detsi, ACS Appl. Energy Mater. 1 (2018) 3198–3205.
[5] J.B. Cook, T.C. Lin, E. Detsi, J.N. Weker, S.H. Tolbert, Nano Lett. 17 (2017) 870–877.
[6] E. Detsi, X. Petrissans, Y. Yan, J.B. Cook, Y.-L. Liang, B. Dunn, S.H. Tolbert, Phys. Rev. Mater. 055404 (2018) 32–37.
[7] O. Ruiz, M. Cochrane, M. Li, Y. Yan, K. Ma, J. Fu, Z. Wang, S.H. Tolbert, V.B. Shenoy, E. Detsi, Adv. Energy Mater. 8 (31) (2018) 1801781.
[8] Y. Ding, M. Chen, MRS Bull. 34 (2009) 569–576.
[9] L. Gan, M. Heggen, R. O'Malley, B. Theobald, P. Strasser, Nano Lett. 13 (2013) 1131–1138.
[10] R.R. Salunkhe, Y.V. Kaneti, Y. Yamauchi, ACS Nano 11 (2017) 5293–5308.
[11] X. Lang, A. Hirata, T. Fujita, M. Chen, Nat. Nanotechnol. 6 (2011) 232–236.
[12] E. Detsi, S. Punzhin, J. Rao, P.R. Onck, J.T.M. De Hosson, ACS Nano 6 (2012) 3734–3744.
[13] J. Weissmüller, R.N. Viswanath, D. Kramer, P. Zimmer, R. Würschum, H. Gleiter, Science 300 (2003) 312–315.
[14] E. Detsi, P. Onck, J.T.M. De Hosson, ACS Nano 7 (2013).
[15] E. Detsi, J.B. Cook, B.K. Lesel, C.L. Turner, Y.-L. Liang, S. Robbennolt, S.H. Tolbert, Energy Environ. Sci. 9 (2016) 540–549.
[16] J. Erlebacher, M.J. Aziz, A. Karma, N. Dimitrov, K. Sieradzki, Nature 410 (2001) 450–453.
[17] E. Detsi, Z. Vuković, S. Punzhin, P.M. Bronsveld, P.R. Onck, J.T.M. De Hosson, CrystEngComm 14 (2012) 5402–5406.
[18] E. Detsi, E. De Jong, a. Zinchenko, Z. Vuković, I. Vuković, S. Punzhin, K. Loos, G. Ten Brinke, H. a. De Raedt, P.R. Onck, J.T.M. De Hosson, Acta Mater 59 (2011) 7488–7497.
[19] E. Detsi, M. Van De Schootbrugge, S. Punzhin, P.R. Onck, J.T.M. De Hosson, Scr. Mater. 64 (2011) 319–322.
[20] H.J. Jin, X.L. Wang, S. Parida, K. Wang, M. Seo, J. Weissmüller, Nano Lett. 10 (2010) 187–194.
[21] M. Hakamada, M. Mabuchi, J. Alloys Compd. 485 (2009) 583–587.
[22] M. Hakamada, M. Mabuchi, Procedia Eng. 81 (2014) 2159–2164.
[23] J. Snyder, I. McCue, K. Livi, J. Erlebacher, J. Am. Chem. Soc. 134 (2012) 8633–8645.
[24] T. Wada, K. Yubuta, A. Inoue, H. Kato, Mater. Lett. 65 (2011) 1076–1078.
[25] T. Wada, T. Ichitsubo, K. Yubuta, H. Segawa, H. Yoshida, H. Kato, Nano Lett. 14 (2014) 4505–4510.
[26] P. Geslin, I. Mccue, J. Erlebacher, A. Karma, Nat. Commun. 6 (2015) 1–19.
[27] T. Wada, J. Yamada, H. Kato, J. Power Sources 306 (2016) 8–16.
[28] J.W. Kim, M. Tsuda, T. Wada, K. Yubuta, S.G. Kim, H. Kato, Acta Mater. 84 (2015) 497–505.
[29] J.W. Kim, T. Wada, S.G. Kim, H. Kato, Mater. Lett. 116 (2014) 223–226.
[30] I. McCue, S. Ryan, K. Hemker, X. Xu, N. Li, M. Chen, J. Erlebacher, Adv. Eng. Mater. 18 (2016) 46–50.
[31] Z. Lu, C. Li, J. Han, F. Zhang, P. Liu, H. Wang, Z. Wang, C. Cheng, L. Chen, A. Hirata, T. Fujita, J. Erlebacher, M. Chen, Nat. Commun. 9 (2018) 276.
[32] M. Kosmidou, M.J. Detisch, T.L. Maxwell, T.J. Balk, M. Eng. (2019) 1–6.
[33] Q. Chen, K. Sieradzki, Nat. Mater. 12 (2013) 1102–1106.
[34] E. Detsi, J.S. Corsi, U.S. Provisional Appl. No. 62/644 972 (2018) (2018).
[35] Z. Qi, J. Weissmüller, ACS Nano 7 (2013) 5948–5954.
[36] T. Fujita, Sci. Technol. Adv. Mater. 18 (2017) 724–740.
[37] Y. Zhang, X. Sun, N. Nomura, T. Fujita, Small (2019) 1805432.
[38] V.A. Beck, J. Ye, J. Biener, W. Chen, C. Zhu, C.M. Friend, E.B. Duoss, C.M. Spadaccini, J. Lattimer, M. Luneau, M.A. Worsley, Z. Qi, Sci. Adv. 4 (2018) eaas9459.
[39] D. Herzog, V. Seyda, E. Wycisk, C. Emmelmann, Acta Mater. 117 (2016) 371–392.
[40] C. Zhu, A.J. Pascall, N. Dudukovic, M.A. Worsley, J.D. Kuntz, E.B. Duoss, C.M. Spadaccini, Annu. Rev. Chem. Biomol. Eng. 10 (2019) annurev-chembioeng060718-030133.
[41] M.A. Turchanin, P.G. Agraval, A.R. Abdulov, Powder Metall. Met. Ceram. 45 (2006) 569–581.
[42] Z. Zak Fang, Sintering of Advanced Materials, 2010.
[43] K. Hoshino, Y. Iijima, K.I. Hirano, Metall. Trans. A 8 (1977) 469–472.
[44] N. Wang, Y. Pan, S. Wu, J. Mater, Sci. Technol 34 (2018) 1162–1171.
[45] S.S. Welborn, E. Detsi, Nanoscale Horizons, 2019.
[46] Y.W. Moon, I.J. Choi, Y.H. Koh, H.E. Kim, J. Eur, Ceram. Soc. 35 (2015) 4623–4627.
[47] E. Schofield, Transact. Inst. Metal Finish 83 (2005) 35–42.
[48] L. Sun, Q. Zhao, J. Xiang, J. Shi, L. Wang, S. Hu, S. Su, Huagong Xuebao/CIESC J. 60 (2009) 444–449.
[49] A. Gali, E.P. George, Intermetallics 39 (2013) 74–78.
[50] Y. Iijima, K. Hirano, K. Sato, Trans. Japan Inst. Met. 18 (1977) 835–842.
[51] L. Boldon, F. Laliberte, L. Liu, Nano Rev. 6 (2015) 25661.
[52] M. Teubner, R. Strey, J. Chem. Phys. 87 (1987) 3195–3200.